Progress In Electromagnetics Research M, Vol. 50, 195–204, 2016

Simulation of High-Altitude Electromagnetic Pulse (HEMP) above Sea Surface

Hong-Cheng Wei and Jean-Fu Kiang

Abstract—High-altitude electromagnetic pulse (HEMP) radiated from both primary and secondary currents, which are induced by a nuclear explosion, is computed by using the Jefimenko's equation. The effects of geomagnetic field is considered in computing the primary current, and the rough sea surface is considered in computing the reflected electric field in the frequency domain. The waveforms of HEMP near sea surface and a few km above it are simulated. The impulse and pulse characteristics are discussed, as well as the variation of peak field magnitude when the observation point is moved away from beneath the burst point.

1. INTRODUCTION

High-altitude electromagnetic pulse (HEMP) was first studied in the early 1960s [1]. Interactions of an EM pulse on complex objects such as aircrafts, satellites, ships, were also investigated [1]. Many HEMP field tests were conducted on electronic systems, military systems and civilian infrastructures [2].

The generation mechanisms and models of HEMP were presented in [3] and [4]. Basically, a nuclear explosion will produce γ rays, which excite air molecules in the upper atmosphere to generate Compton electrons. These Compton electrons move in parallel with the γ rays and gyrate around the geomagnetic field lines. Secondary electrons are induced when the Compton electrons ionize air molecules in their way. Both the Compton (primary) current and the secondary current contribute to the radiated electric field, which forms an HEMP.

An HEMP may cause damages to electronic equipments on board of maritime ships [5]. Due to the operational environment, the electrically conductive superstructure, topside hardware and antenna systems, the evaluation of potential threat on ships by an HEMP attack becomes complicated [6]. The VHF radios for communications and container cranes on ships are also vulnerable to an HEMP attack [7].

Both pulse and continuous-wave (CW) simulators were used for evaluating the integrity of electromagnetic shields in large objects like aircrafts, ships and ground-based communications systems. Continuous-wave test methods for such tasks were reviewed in [8]. A series of CW illumination measurements, up to 100 MHz, on ships were made in 1992, to measure possible penetration through the deck by using a single-wire transmission line. For larger ships or for ships with openings on the hull, a complete illumination is needed.

Countermeasures against HEMP attacks on ships were studied [9–12]. The interaction and coupling phenomena of HEMP with the antennas, cables, and mast structures of a ship was estimated [13]. In [14], a method was presented to simulate the electric fields at different frequency components of an HEMP, with an IEC-61000-2-9 waveform radiated upon a ship's board from vertical and oblique directions, respectively.

Received 19 August 2014, Accepted 16 April 2016, Scheduled 11 October 2016
* Corresponding author: Jean-Fu Kiang (jfkiang@ntu.edu.tw).
The authors are with the Department of Electrical Engineering and the Graduate Institute of Communication Engineering, National Taiwan University, Taipei 106, Taiwan.

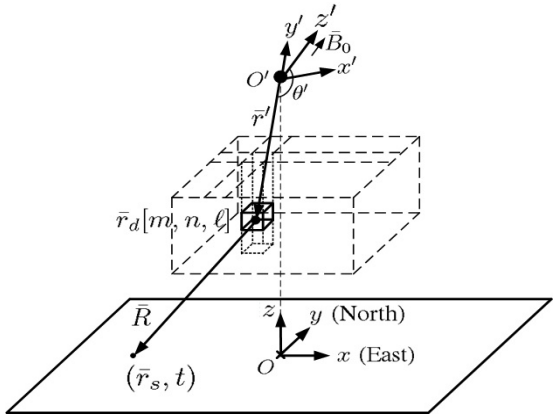

Figure 1. Coordinate systems defined to simulate an HEMP event.

In this work, the electric field of an HEMP is simulated near the sea surface and a few km above the sea level. The Jefimenko's equation is used to compute the radiation from the induced currents. The effects of geomagnetic field and reflection by rough sea surface are also included. This paper is organized as follows: The theoretical model is presented in Section 2, simulation results are discussed in Section 3, and some conclusions are drawn in Section 4.

2. THEORETICAL MODEL

Figure 1 shows the coordinate systems defined to simulate the electric fields of an HEMP caused by a nuclear explosion. The origin O' represents the burst point, which is directly above the origin O, with $\overline{OO'} = \hat{z}h$. The primary current density, under the effects of geomagnetic field, can be expressed as [3]

$$\begin{aligned}
J_{\mathrm{pri},r'}(\bar{r}', t') &\simeq -e\zeta v_0 g(\bar{r}') \int_0^{R_\gamma/v_0} d\tau'' \left(\cos^2\theta' + \sin^2\theta' \cos\omega_L\tau''\right) \\
&\quad f\left(\tau' - (1-\beta\cos^2\theta)\tau'' + \beta\sin^2\theta \frac{\sin\omega_L\tau''}{\omega_L}\right) \\
J_{\mathrm{pri},\theta'}(\bar{r}', t') &\simeq -e\zeta v_0 g(\bar{r}') \int_0^{R_\gamma/v_0} d\tau'' \sin\theta'\cos\theta' \left(\cos\omega_L\tau'' - 1\right) \\
&\quad f\left(\tau' - (1-\beta\cos^2\theta')\tau'' + \beta\sin^2\theta' \frac{\sin\omega_L\tau''}{\omega_L}\right) \\
J_{\mathrm{pri},\phi'}(\bar{r}', t') &\simeq -e\zeta v_0 g(\bar{r}') \int_0^{R_\gamma/v_0} d\tau'' \sin\theta' \sin\omega_L\tau'' \\
&\quad f\left(\tau' - (1-\beta\cos^2\theta')\tau'' + \beta\sin^2\theta' \frac{\sin\omega_L\tau''}{\omega_L}\right) \qquad (1)
\end{aligned}$$

where $e = 1.6 \times 10^{-19}$ coul is the basic charge unit, $\zeta \simeq 1$, $v_0 = 0.95c$ m/s is the mean velocity of primary electrons; $\omega_L = eB_0/(\gamma_L m_e)$ is the cyclotron frequency, with $\gamma_L = 1/\sqrt{1-\beta^2}$ and $\beta = v_0/c$; $t' = t - R/c$, $\tau' = t' - r'/c$ and $\tau'' = t' - t''$; t is the time to observe the electric fields above sea surface, with the burst occurring at $t = 0$; t' is the time to observe the primary current in the source region, t'' is the time when a γ ray interacts with air molecules in the source region; $R_\gamma \simeq 3 \times 10^2 \rho_0/\rho$ (cm) is the mean distance a primary electron travels in the atmosphere; ρ and ρ_0 are the air density at the height of interest and on the sea surface, respectively. The functions $f(t')$ and $g(\bar{r}')$ can be represented

as [3, 15]

$$f(t') = \frac{e^{-\alpha_1/t'-\alpha_2 t'}u(t')}{\int_0^\infty dt' e^{-\alpha_1/t'-\alpha_2 t'}}, \qquad g(\bar{r}') = \frac{Y_\gamma}{E_{\text{ray}}} \frac{\exp\left\{-\int dr'/\ell_m\right\}}{4\pi r'^2 \ell_m}$$

where $Y_\gamma = 0.001Y$ (ton) is the γ ray yield; Y (ton) is the yield of the explosive; E_{ray} (MeV) is the mean γ ray energy, which is set to 1.6 in this work; $\ell_m \simeq 3 \times 10^4 \rho_0/\rho$ (cm) is the mean-free-path of primary electrons; and $\alpha_1 = 2 \times 10^{-8}$ s and $\alpha_2 = 2 \times 10^8$ s^{-1} are two empirical parameters. Fig. 2 shows a typical pulse waveform $f(t')$ [15], which is used in the subsequent simulations.

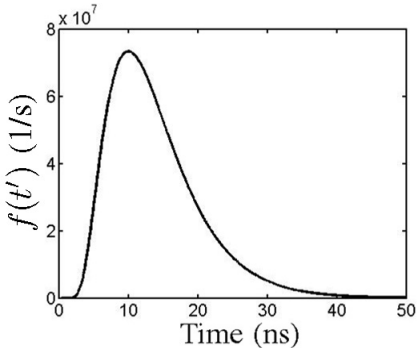

Figure 2. A typical pulse waveform $f(t')$ [15].

The secondary current density can be expressed as $\bar{J}_{\text{sec}} = \sigma \bar{E}$, where

$$\sigma(\bar{r}', t', |\bar{E}|) = e\mu_e(\bar{r}', |\bar{E}|) n_{\text{sec}}(\bar{r}', t') \tag{2}$$

is the effective conductivity [3], $m_e = 9.1 \times 10^{-31}$ kg is the electron mass, $\nu_c = 4 \times 10^{12} \rho/\rho_0\,(\text{s}^{-1})$ is the collisional frequency, and the number density of secondary electrons, in the presence of geomagnetic field, can be expressed as [3, 16]

$$n_{\text{sec}}(\bar{r}', t') \simeq -q \frac{v_0}{R_\alpha} g(\bar{r}') \int_{-\infty}^{\tau} e^{-k_1(\tau-\tau')} d\tau' \int_0^{R_\alpha/v_0} d\tau'' f\left(\tau' - (1-\beta\cos^2\theta)\tau'' + \beta \sin^2\theta \frac{\sin\omega_L \tau''}{\omega_L}\right) \tag{3}$$

where $k_1 = 10^8(\rho/\rho_0)^2\,\text{s}^{-1}$ is the attachment rate of an electron to an oxygen molecule [4].

By alternately updating the electric field and the air conductivity, the electric field is iterated as [17]

$$E_{r'}^{(n)}(\bar{r}', \tau') = -\frac{1}{\epsilon_0} \int_0^{\tau'} d\tau'' J_{\text{pri},r'}(\bar{r}', \tau'') \exp\left\{\frac{1}{\epsilon_0} \int_{\tau'}^{\tau''} d\tau''' \sigma^{(n-1)}(\bar{r}', \tau''', |\bar{E}^{(n-1)}|)\right\} \tag{4}$$

$$E_{\alpha}^{(n)}(\bar{r}', \tau') = -\frac{c\mu_0}{2} \frac{1}{r'} \int_0^{r'} dr'' r'' J_{\text{pri},\alpha}(\bar{r}'', \tau') \exp\left\{-\frac{c\mu_0}{2} \int_{r''}^{r'} dr''' \sigma^{(n-1)}(\bar{r}''', \tau', |\bar{E}^{(n-1)}|)\right\} \tag{5}$$

with $n = 2, 3, \ldots$, until $E^{(n)}$ converges. The convergent electric field is then substituted into (2) to obtain the convergent air conductivity.

The electric field near the sea surface, induced by the electric current, can be calculated by using the Jefimenko's equation as [18]

$$\bar{E}_i(\bar{r}_s, t) = \frac{1}{4\pi\epsilon_0} \iiint_{V'} d\bar{r}_d \left[-\frac{\bar{J}(\bar{r}_d, t')}{cR^2} + 2\bar{R}\frac{\bar{J}(\bar{r}_d, t') \cdot \bar{R}}{cR^4} + \bar{R}\frac{\partial \bar{J}(\bar{r}_d, t')/\partial t' \cdot \bar{R}}{c^2 R^3} - \frac{\partial \bar{J}(\bar{r}_d, t')/\partial t'}{c^2 R}\right] \tag{6}$$

where $\bar{R} = \bar{r}_s - \bar{r}_d$. Eq. (6) can be transformed to the frequency domain as

$$\bar{E}_i(\bar{r}_s, \omega) = \frac{1}{4\pi\epsilon_0} \iiint_{V'} d\bar{r}_d \left[-\frac{\bar{J}(\bar{r}_d, \omega)}{cR^2} + 2\bar{R}\frac{\bar{J}(\bar{r}_d, \omega) \cdot \bar{R}}{cR^4} + \bar{R}\frac{j\omega \bar{J}(\bar{r}_d, \omega) \cdot \bar{R}}{c^2 R^3} - \frac{j\omega \bar{J}(\bar{r}_d, \omega)}{c^2 R}\right] e^{-j\omega R/c} \tag{7}$$

where

$$\bar{E}_i(\bar{r}_s,t)=\frac{1}{2\pi}\int_{-\infty}^{\infty}d\omega\bar{E}_i(\bar{r}_s,\omega)e^{j\omega t} \tag{8}$$

The current density in the source region is transformed to $\bar{J}(\bar{r}_d,\omega)=e^{-j\omega\tau'/c}\bar{J}_0(\bar{r}_d,\omega)$, where

$$\bar{J}_0(\bar{r}_d,\omega)=\int_0^{\infty}d\tau'\bar{J}(\bar{r}_d,\tau')e^{-j\omega\tau'} \tag{9}$$

By substituting (9) into (7), we obtain

$$\bar{E}_i(\bar{r}_s,\omega)=\frac{1}{4\pi\epsilon}\iiint\limits_{V'}d\bar{r}_d\left[-\frac{\bar{J}_0(\bar{r}_d,\omega)}{cR^2}+2\bar{R}\frac{\bar{J}_0(\bar{r}_d,\omega)\cdot\bar{R}}{cR^4}+\bar{R}\frac{j\omega\bar{J}_0(\bar{r}_d,\omega)\cdot\bar{R}}{c^2R^3}-\frac{j\omega\bar{J}_0(\bar{r}_d,\omega)}{c^2R}\right]e^{-j\omega(r'+R)/c} \tag{10}$$

which can be further decomposed as $\bar{E}_i(\bar{r}_s,\omega)=\bar{E}_i^{\mathrm{TE}}(\bar{r}_s,\omega)+\bar{E}_i^{\mathrm{TM}}(\bar{r}_s,\omega)$.

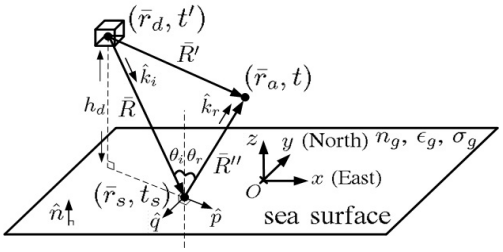

Figure 3. Schematic of incident and reflected fields above sea surface.

The effects of rough sea surface on maritime communications were studied in [19–23]. Fig. 3 shows the schematic of incident and reflected fields above sea surface, caused by currents in a specific cube in the source region. The reflected field at $\bar{r}_s$ can be expressed in terms of the TE and TM components as

$$\bar{E}_r(\bar{r}_s,\omega)=\left[\Gamma_{\mathrm{TE}}\hat{q}\hat{q}+\Gamma_{\mathrm{TM}}\left(\hat{p}\hat{p}-\hat{z}\hat{z}\right)\right]\cdot\bar{E}_i(\bar{r}_s,\omega) \tag{11}$$

where $\hat{q}=\hat{x}\sin\theta_1-\hat{y}\cos\theta_1$, $\hat{p}=\hat{x}\cos\theta_1+\hat{y}\sin\theta_1$, $\theta_1=\cos^{-1}(R_x/\sqrt{R_x^2+R_y^2})$; and the reflection coefficients of the TE and TM components on a rough sea surface can be expressed as

$$\Gamma_{\mathrm{TE}}(\bar{r}_s,\bar{r}_d,\omega)=\rho_{\mathrm{MB}}\frac{k_{az}-k_{gz}}{k_{az}+k_{gz}},\qquad\Gamma_{\mathrm{TM}}(\bar{r}_s,\bar{r}_d,\omega)=\rho_{\mathrm{MB}}\frac{j\omega\epsilon_0(k_{gz}-\epsilon_{rg}k_{az})-\sigma_gk_{az}}{j\omega\epsilon_0(k_{gz}+\epsilon_{rg}k_{az})+\sigma_gk_{az}} \tag{12}$$

where $\rho_{\mathrm{MB}}=e^{-\xi^2/2}I_0(\xi^2/2)$ is the Miller-Brown roughness reduction factor [24, 25], $I_0(\alpha)$ is the zeroth-order modified Bessel function of the first kind, $\xi=2k_a\sigma_h\sin\chi$, $\chi=\pi/2-\theta_i$, $\sigma_h=5.1\times10^{-3}U_{10}^2$ is the standard deviation of sea-surface profile, U_{10} is the wind speed at 10 m above the sea level, $\theta_i=\theta_r=\cos^{-1}\left(-\hat{z}\cdot\hat{R}\right)$, $k_a=\omega\sqrt{\mu_0\epsilon_0}$, $k_g=\omega\sqrt{\mu_0\epsilon_0\epsilon_{rg}}\sqrt{1+\sigma_g/(j\omega\epsilon_0\epsilon_{rg})}$, $k_{az}=k_a\cos\theta_i$, $k_{ap}=k_a\sin\theta_i$, and $k_{gz}=\sqrt{k_g^2-k_{ap}^2}=-j\alpha_g+\beta_g$.

The reflected field at $\bar{r}_s$, contributed by all the currents in the source region, can thus be expressed as

$$\bar{E}_r(\bar{r}_s,\omega)=\frac{1}{4\pi\epsilon_0}\iiint\limits_{V'}d\bar{r}_d\bar{E}_{r0}(\bar{r}_s,\bar{r}_d,\omega)e^{-j\omega(r'+R)/c} \tag{13}$$

with

$$\begin{aligned}\bar{E}_{r0}(\bar{r}_s,\bar{r}_d,\omega)\;=\;&\left[\Gamma_{\mathrm{TE}}\hat{q}\hat{q}+\Gamma_{\mathrm{TM}}\left(\hat{p}\hat{p}-\hat{z}\hat{z}\right)\right]\\&\left[-\frac{\bar{J}_0(\bar{r}_d,\omega)}{cR^2}+2\bar{R}\frac{\bar{J}_0(\bar{r}_d,\omega)\cdot\bar{R}}{cR^4}+\bar{R}\frac{j\omega\bar{J}_0(\bar{r}_d,\omega)\cdot\bar{R}}{c^2R^3}-\frac{j\omega\bar{J}_0(\bar{r}_d,\omega)}{c^2R}\right]\end{aligned} \tag{14}$$

Finally, the total electric field at $(\bar{r}_a, t)$ can be expressed as

$$\bar{E}(\bar{r}_a, t) = \bar{E}_i(\bar{r}_a, t) + \bar{E}_r(\bar{r}_a, t)$$

where

$$\bar{E}_r(\bar{r}_a, t) = \frac{1}{4\pi\epsilon_0} \iiint_{V'} d\bar{r}_d \frac{1}{2\pi} \int_{-\infty}^{\infty} d\omega \bar{E}_{r0}(\bar{r}_s, \bar{r}_d, \omega) e^{j\omega[t-(r'+R+R'')/c]} = \frac{1}{4\pi\epsilon_0} \iiint_{V'} d\bar{r}_d \bar{E}_{r0}(\bar{r}_s, \bar{r}_d, \tau') \quad (15)$$

$\tau' = t - (r' + R + R'')/c$, $\bar{R}' = \bar{r}_a - \bar{r}_d$, $\bar{R}'' = \bar{r}_a - \bar{r}_s$, and $\bar{k}_r \cdot \bar{R}'' = k_a R'' = \omega R''/c$.

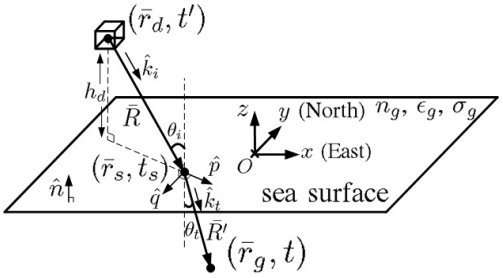

Figure 4. Schematic to compute the electric field beneath sea surface.

Figure 4 shows the schematic to compute the electric field beneath the sea surface, contributed by currents in a cube centered at $\bar{r}_d$. The transmitted field at $\bar{r}_g$ can be expressed as

$$\bar{E}_t(\bar{r}_g, \omega) = \left[T_{\rm TE} \hat{q}\hat{q} + T_{\rm TM} \left(\frac{\cos\theta_t}{\cos\theta_i} \hat{p}\hat{p} + \frac{\sin\theta_t}{\sin\theta_i} \hat{z}\hat{z} \right) \right] \bar{E}_i(\bar{r}_s, \omega) e^{-j\bar{k}_t \cdot \bar{R}_g} \quad (16)$$

where $\bar{R}_g = \bar{r}_g - \bar{r}_s$, $\bar{k}_t \cdot \bar{R}_g \simeq \omega R_g/v_g + j\alpha_g R_{gz}$, and the transmission coefficients of the TE and TM components through rough sea surface are approximated as

$$T_{\rm TE}(\bar{r}_s, \bar{r}_g, \omega) = \rho_{\rm MB} \frac{2k_{az}}{k_{az} + k_{gz}}, \qquad T_{\rm TM}(\bar{r}_s, \bar{r}_g, \omega) = \rho_{\rm MB} \frac{\cos\theta_i}{\cos\theta_t} \frac{2j\omega\epsilon_0 k_{gz}}{j\omega(\epsilon_g k_{az} + \epsilon_0 k_{gz}) + \sigma_g k_{az}}$$

Thus, the transmitted field at $\bar{r}_g$, contributed by all the currents in the source region, can be expressed as

$$\bar{E}_t(\bar{r}_g, \omega) = \frac{1}{4\pi\epsilon_0} \iiint_{V'} d\bar{r}_d \bar{E}_{t0}(\bar{r}_g, \omega) e^{-j\omega[(r'+R)/c + R_g/v_g]} e^{\alpha_g R_{gz}}$$

with

$$\begin{aligned} \bar{E}_{t0}(\bar{r}_g, \omega) \;=\; & \left[T_{\rm TE} \hat{q}\hat{q} + T_{\rm TM} \left(\frac{\cos\theta_t}{\cos\theta_i} \hat{p}\hat{p} + \frac{\sin\theta_t}{\sin\theta_i} \hat{z}\hat{z} \right) \right] \\ & \cdot \left[-\frac{\bar{J}_0(\bar{r}_d, \omega)}{cR^2} + 2\bar{R} \frac{\bar{J}_0(\bar{r}_d, \omega) \cdot \bar{R}}{cR^4} + \bar{R} \frac{j\omega \bar{J}_0(\bar{r}_d, \omega) \cdot \bar{R}}{c^2 R^3} - \frac{j\omega \bar{J}_0(\bar{r}_d, \omega)}{c^2 R} \right] \end{aligned} \quad (17)$$

Finally, the time-domain transmitted field at $\bar{r}_g$ can be expressed as

$$\begin{aligned} \bar{E}_t(\bar{r}_g, t) \;=\; & \frac{1}{4\pi\epsilon_0} \iiint_{V'} d\bar{r}_d \frac{1}{2\pi} \int_{-\infty}^{\infty} d\omega \bar{E}_{t0}(\bar{r}_g, \bar{r}_d, \omega) e^{j\omega[t-(r'+R)/c - R_g/v_g]} e^{\alpha_g R_{gz}} \\ =\; & \frac{1}{4\pi\epsilon_0} \iiint_{V'} d\bar{r}_d \bar{E}_{t0}(\bar{r}_g, \bar{r}_d, \tau') \end{aligned} \quad (18)$$

where $\tau' = t - (r' + R)/c - R_g/v_g$.

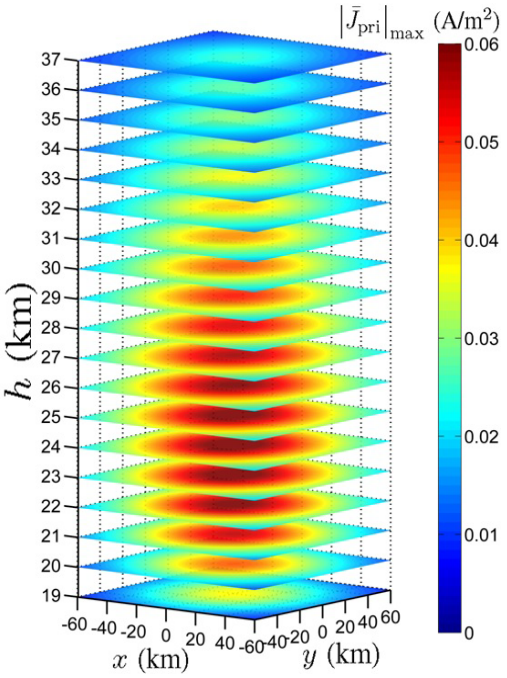

Figure 5. Distribution of $|\bar{J}_{\rm pri}|_{\rm max}$ in the source region, with HOB at $h = 100\,$km.

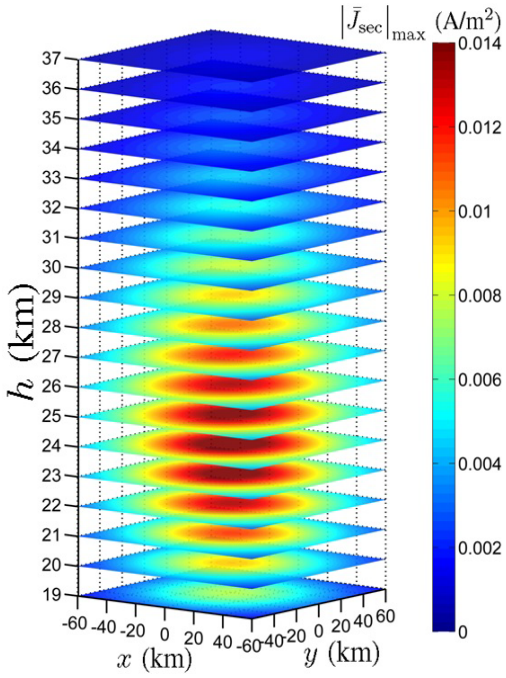

Figure 6. Distribution of $|\bar{J}_{\rm sec}|_{\rm max}$ in source region, with HOB at $h = 100\,$km.

3. SIMULATIONS AND DISCUSSIONS

Figure 5 shows the spatial distribution of the maximum amplitude of $|\bar{J}_{\rm pri}|$ in the source region, with the height-of-burst (HOB) at 100 km. The yield of explosive is assumed to be 10 kiloton; $\bar{B}_0$ is along the $\hat{y}$ direction, with magnitude of 0.4 Gauss.

Figure 6 shows the distribution of the maximum amplitude of $|\bar{J}_{\rm sec}|$ in the source region. Fig. 7 shows the distribution of $|\partial \bar{J}_{\rm tot}/\partial t'|_{\rm max}$, where $\partial \bar{J}_{\rm tot}/\partial t'$ is the time derivative of $\bar{J}_{\rm tot}$. In the subsequent simulations, the length, width and height of the effective source region are chosen to be 102 km, 102 km and 18 km, respectively; and the bottom of the source region is at $h_b = 19\,$km above the sea surface.

Figure 8 shows the impulse waveform of E_{ix} observed at $(x_a, y_a, z_a) = (0, 0, 20)\,$m, with the peak value of $-12,940\,$V/m. Since the geomagnetic field points in the $\hat{y}$ direction, making the electrons move in the x-z plane, thus no E_{iy} component is observed.

Figure 9 shows the pulse waveform of E_{iz} at $(x_a, y_a, z_a) = (0, 0, 20)\,$m, with the peak value of $-37.3\,$V/m. The distribution of primary current is symmetrical with respect to $\overline{OO'}$ shown in Fig. 1. At observation points along $\overline{OO'}$, the z-component of electric field radiated by the primary current is zero due to symmetry of the primary current distribution, hence the waveform of E_{iz} shows no impulse characteristics.

Figure 10 shows the impulse waveform of E_{rx} at $(x_a, y_a, z_a) = (0, 0, 20)\,$m. The peak values of E_{rx} at $U_{10} = 0, 5$ and 10 m/s are 12,820, 12,523 and 9,052 V/m, respectively. The reflected field at $U_{10} = 5\,$m/s is almost the same as that at $U_{10} = 0\,$m/s. The waveforms of E_{ry} and E_{rz} show no impulse characteristics for the same reason as the incident field. Most spectral components of the incident field are below 100 MHz. At low or mild wind speeds, the Miller-Brown roughness reduction factor ($\rho_{\rm MB}$) is close to unity. Take $U_{10} = 5\,$m/s for example, $\rho_{\rm MB} = 1$, 0.9993 and 0.9324 at $f = 1$, 10 and 100 MHz, respectively, with $\theta_i = 45°$. At $U_{10} = 10\,$m/s and $\theta_i = 45°$, we have $\rho_{\rm MB} = 0.9999$, 0.9887 and 0.4323 at $f = 1$, 10 and 100 MHz, respectively. Hence, the waveform of the reflected field appears similar to that of the incident field.

Figure 11 shows the impulse waveform of E_x at $(x_a, y_a, z_a) = (0, 0, 5)\,$m. The E_{rx} begins to rise right after the fall of E_{ix}. Thus, the field magnitude during this transition period changes more rapidly

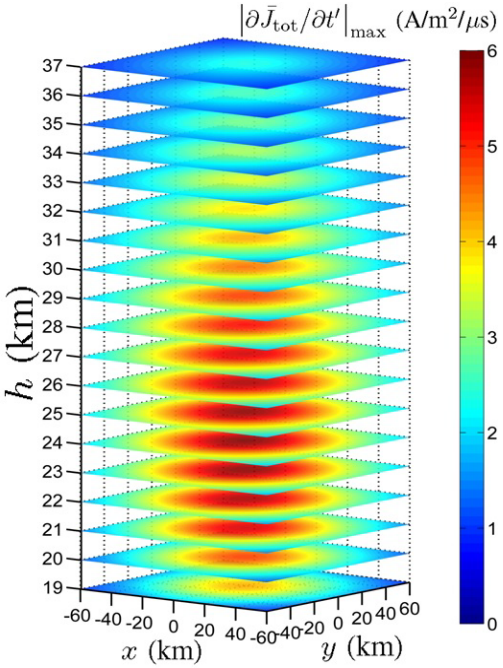

Figure 7. Distribution of $|\partial \bar{J}_{\rm tot}/\partial t'|_{\rm max}$ in the source region, with HOB at $h = 100$ km.

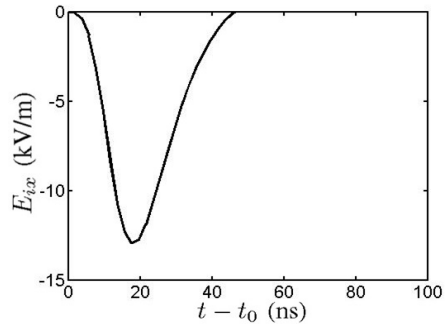

Figure 8. Waveform of E_{ix} impulse at $(x_a, y_a, z_a) = (0, 0, 20)$ m, $t_0 = 333.26$ µs.

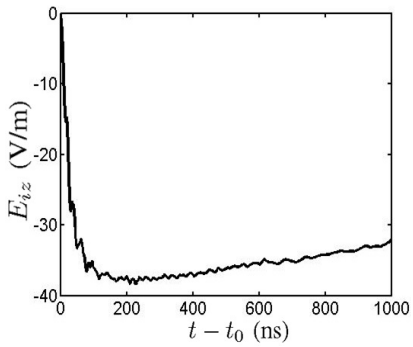

Figure 9. Waveform of E_{iz} pulse at $(x_a, y_a, z_a) = (0, 0, 20)$ m, $t_0 = 333.26$ µs.

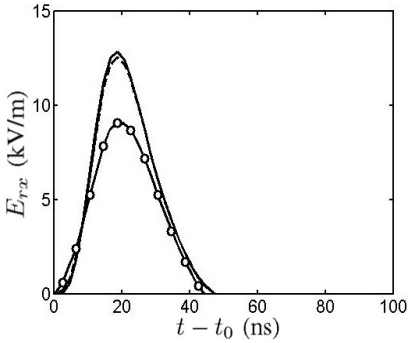

Figure 10. Waveforms of E_{rx} impulse at $(x_a, y_a, z_a) = (0, 0, 20)$ m, $t_0 = 333.4$ µs; ——: $U_{10} = 0$, − − −: $U_{10} = 5$ m/s, −○−: $U_{10} = 10$ m/s.

than that at $z_a = 20$ m.

Figure 12 shows the impulse waveforms of E_{ix} at $(x_a, y_a, z_a) = (0, 0, 2)$ km. The peak value of E_{ix} is $-13,210$ V/m, which is slightly larger than that at $(x_a, y_a, z_a) = (0, 0, 20)$ m because the former is observed at a shorter distance from the source region than the latter.

Figure 13 shows the pulse waveform of E_{iz} at $(x_a, y_a, z_a) = (0, 0, 2)$ km, with the peak value of -42.2 V/m.

Figure 14 shows the impulse waveform of E_{rx} at $(x_a, y_a, z_a) = (0, 0, 2)$ km. The peak values are 13,462, 13,148 and 9,477 V/m, at $U_{10} = 0, 5$ and 10 m/s, respectively. Similar to the observation in Fig. 10, the peak value at $U_{10} = 10$ m/s is smaller than those at lower wind speeds.

Figure 15 shows the distributions of impulse amplitude of E_x, E_y and E_z, respectively, along the x_a axis, with $(y_a, z_a) = (0, 20)$ m and $U_{10} = 10$ m/s. The E_z component shows impulse characteristics at $x_a \neq 0$ where the contribution from the primary currents in the source region is not completely canceled out. The E_y component shows no impulse characteristics at $x_a \neq 0$ due to symmetry of the primary

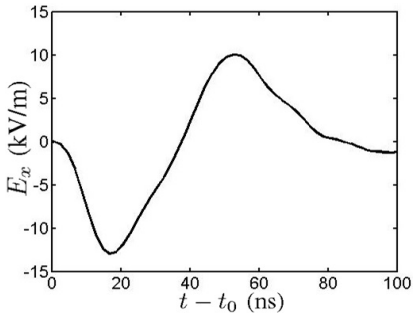

Figure 11. Waveform of E_x impulse at $(x_a, y_a, z_a) = (0, 0, 5)$ m with $t_0 = 333.3\,\mu$s, $U_{10} = 10$ m/s.

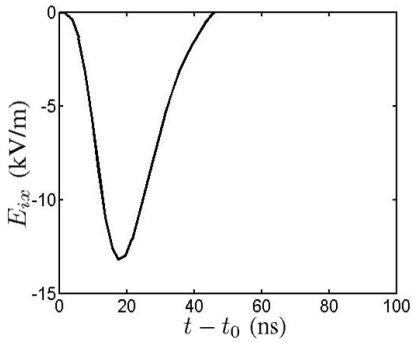

Figure 12. Waveforms of E_{ix} impulse at $(x_a, y_a, z_a) = (0, 0, 2)$ km, $t_0 = 326.6\,\mu$s.

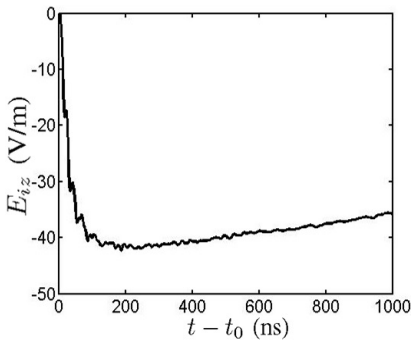

Figure 13. Waveform of E_{iz} pulse at $(x_a, y_a, z_a) = (0, 0, 2)$ km, $t_0 = 326.6\,\mu$s.

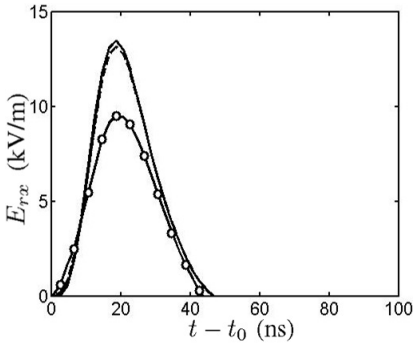

Figure 14. Waveforms of E_{rx} impulse at $(x_a, y_a, z_a) = (0, 0, 2)$ km, $t_0 = 340\,\mu$s; ——: $U_{10} = 0$, − − −: $U_{10} = 5$ m/s, −○−: $U_{10} = 10$ m/s.

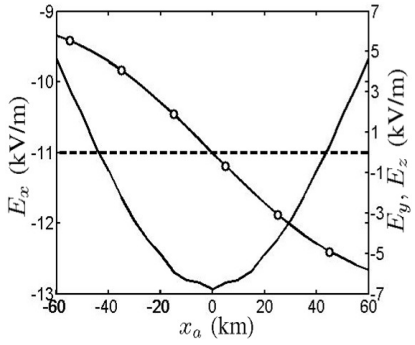

Figure 15. Impulse amplitude of total electric field along x_a axis, $(y_a, z_a) = (0, 20)$ m and $U_{10} = 10$ m/s. ——: E_x, − − −: E_y, − ○ −: E_z.

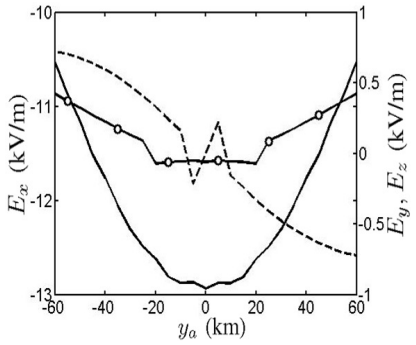

Figure 16. Impulse amplitude of total electric field along y_a axis, $(x_a, z_a) = (0, 20)$ m and $U_{10} = 10$ m/s. ——: E_x, − − −: E_y, − ○ −: E_z.

current distribution with respect to the xz-plane.

Figure 16 shows the distributions of impulse amplitude of E_x, E_y and E_z, respectively, along the y_a axis, with $(x_a, z_a) = (0, 20)$ m and $U_{10} = 10$ m/s. The amplitude of E_y increases with $|y_a|$ because the difference of contribution from primary currents in the source region with $y > y_a$ and that with $y < y_a$ increases with $|y_a|$. The E_z component shows impulse characteristics at $y_a \neq 0$ for the same reason that explains Fig. 15.

4. CONCLUSION

A complete model of HEMP generation, including the effects of geomagnetic field and reflection from sea surface, has been established to simulate the HEMP waveforms above sea surface. Both pulse and impulse characteristics are observed and analyzed. Simulations results at 20 m and 2 km, respectively, above sea level are also compared. The effects of rough sea surface under different wind speeds are considered. Reflected components of an HEMP near the sea surface may impose stronger threat than the incident HEMP alone. Various parameters characterizing HEMPs have been presented and analyzed based on the simulation results.

REFERENCES

1. Prather, W. D., D. V. Giri, R. L. Gardner, F. M. Tesche, R L. Hutchins, and J. C. Giles, "Early developments in sensors and simulators at the Air Force Weapons Laboratory," *IEEE Trans. Electromagn. Compat.*, Vol. 55, No. 3, 431–439, June 2013.
2. Sabath, F. and S. Potthast, "Tolerance values and the confidence level for high-altitude electromagnetic pulse (HEMP) field tests," *IEEE Trans. Electromagn. Compat.*, Vol. 55, No. 3, 518–525, June 2013.
3. Karzas, W. J. and R. Latter, "Detection of the electromagnetic radiation from nuclear explosions in space," *Phys. Rev.*, Vol. 137, No. 5B, 1369–1378, 1965.
4. Longmire, C. L., "On the electromagnetic pulse produced by nuclear explosions," *IEEE Trans. Electromagn. Compat.*, Vol. 20, No. 1, 3–12, Feb. 1978.
5. Jump, M. E. and W. C. Emberson, "Ship EMP survivability trials-reply," *Naval Eng. J.*, Vol. 103, No. 4, 119–120, July 1991.
6. Department of Defense Standard Practice, "Shipboard bonding, grounding, and other techniques for electromagnetic compatibility, electromagnetic pulse (EMP) mitigation, and safety," *MIL-STD-1310H (NAVY)*, September 2009.
7. Graham, W. R., J. S. Foster, E. Gjelde, R. J. Hermann, H. M. Kluepfel, R. L. Lawson, G. K. Soper, L. L. Wood, and J. B. Woodart, "Report of the commission to assess the threat to the US from an electromagnetic pulse (EMP) attack," *US Congress Commission*, 2008.
8. Prather, W. D., J. Cafferky, L. Ortiz, and J. Anderson, "CW measurements of electromagnetic shields," *IEEE Trans. Electromagn. Compat.*, Vol. 55, No. 3, 500–507, June 2013.
9. Perez, R., *Handbook of Electromagnetic Compatibility*, Academic Press, 1st Edition, 1995.
10. Said, M. O., "Theory and practice of total ship survivability for ship design," *Naval Eng. J.*, Vol. 107, No. 4, 191–203, July 1995.
11. Haag, K., et al., "EMP design guidelines for naval ship systems," *IIT Res. Inst.*, Chicago IL, 1975.
12. Ianoz, M., B. Nicoara, and W. Radasky, "Modeling of an EMP conducted environment," *IEEE Trans. Electromagn. Compat.*, Vol. 38, No. 3, 400–413, August 1996.
13. Deadrick, F. J., et al., "EMP coupling to ships," *Lawrence Livermore Lab.*, 1980.
14. Cai, M., H. Wan, S. Tang, and P. Xu, "Research on electromagnetic environment above board of ship radiated by HEMP," *Int. Conf. Electron. Mech. Eng. Info. Technol.*, 3442–3444, August 2011.
15. Seiler, Jr., L. W., "A calculational model for high altitude EMP," Air Force Inst. Technol., Wright-Patterson Air Force Base, Ohio, March 1975.
16. Meng, C., "Numerical simulation of the HEMP environment," *IEEE Trans. Electromagn. Compat.*, Vol. 55, No. 3, 440–445, June 2013.
17. Wei, H.-C. and J.-F. Kiang, "Near-ground transient field of a high-altitude electromagnetic pulse (HEMP) considering nonlinear air conductivity and ground reflection," *Progress In Electromagnetics Research M*, Vol. 48, 45–54, 2016.
18. Jefimenko, O. D., *Electromagnetic Retardation and Theory of Relativity*, Electret Scientific, 2004.

19. Ohmori, S., A. Irimata, H. Morikawa, K. Kondo, Y. Hase, and S. Miura, "Characteristics of sea reflection fading in maritime satellite communications," *IEEE Trans. Antennas Propagat.*, Vol. 33, No. 8, 838–845, August 1985.
20. Sobieski, P., A. Guissard, C. Baufays, and P. Siraut, "Sea surface scattering calculations in maritime satellite communications," *IEEE Trans. Commun.*, Vol. 41, No. 10, 1525–1533, October 1993.
21. Benhmammouch, O., A. Khenchaf, and N. Caouren, "Modelling roughness effects on propagation of electromagnetic waves in a maritime environment: A hybrid approach," *IET Radar, Sonar, Navig.*, Vol. 5, No. 9, 1018–1025, December 2011.
22. Vicen-Bueno, R., R. Carrasco-Alvarez, M. P. Jarabo-Amores, J. C. Nieto-Borge, and M. Rosa-Zurera, "Ship detection by different data," *IET Radar, Sonar, Navig.*, Vol. 5, No. 2, 144–154, October 2011.
23. Sevgi, L., "Target reflectivity and RCS interactions in integrated maritime surveillance systems based on surface-wave high-frequency radars," *IEEE Antennas Propagat. Mag.*, Vol. 43, No. 1, 36–51, February 2001.
24. Levy, M., *Parabolic Equation Methods for Electromagnetic Wave Propagation*, Inst. Electr. Eng., 2000.
25. Miller, A. R., R. M. Brown, and E. Vegh, "New derivation for the rough-surface reflection coefficient and for the distribution of sea-wave elevations," *IEE Proc. H: Microwaves Opt. Antennas*, Vol. 131, No. 2, 114–116, 1984.